ICRR-332-94-27

Fermilab Library
0 1160 0072158 3

ISSN 1340-3745

ICRR

ICRR-Report-332-94-27

Measurement of the Solar and Atmospheric Neutrino Fluxes in Kamiokande

FERMILAB
JAN 26 1995
LIBRARY

T Kajita

NAME	I D No.	M.S.

RETURN TO FERMILAB LIBRARY

(December 1994)

Lecture Presented at the 5th BCSPIN Summer School in Physics, Kathmandu, Nepal, May-June, 1994.

INSTITUTE FOR COSMIC RAY RESEARCH
UNIVERSITY OF TOKYO
3-2-1 Midori-cho, Tanashi, Tokyo 188, Japan

1 Introduction

The solar neutrino problem has been with us for more than 20 years. There is also a problem in the atmospheric ν_μ/ν_e flux ratio for more than 5 years. With recent data from various underground experiments, it is getting more and more difficult to explain these experimental results using only known physics. Kamiokande provides data for these two problems.

The Kamiokande detector is a 4.5-kton water Cerenkov detector located at a depth of 2700 meters water equivalent in the Kamioka mine in Japan. It consists of two layers of water, each instrumented with two dimensional arrays of 50 cm diameter photomultiplier tubes (PMTs) covering all surfaces. The inner volume of water constitutes an inner-detector, which detects Cerenkov photons radiated by relativistic charged particles. The outer layer surrounds the inner-detector constituting a 4π solid-angle anti-counter. See Fig. 1.

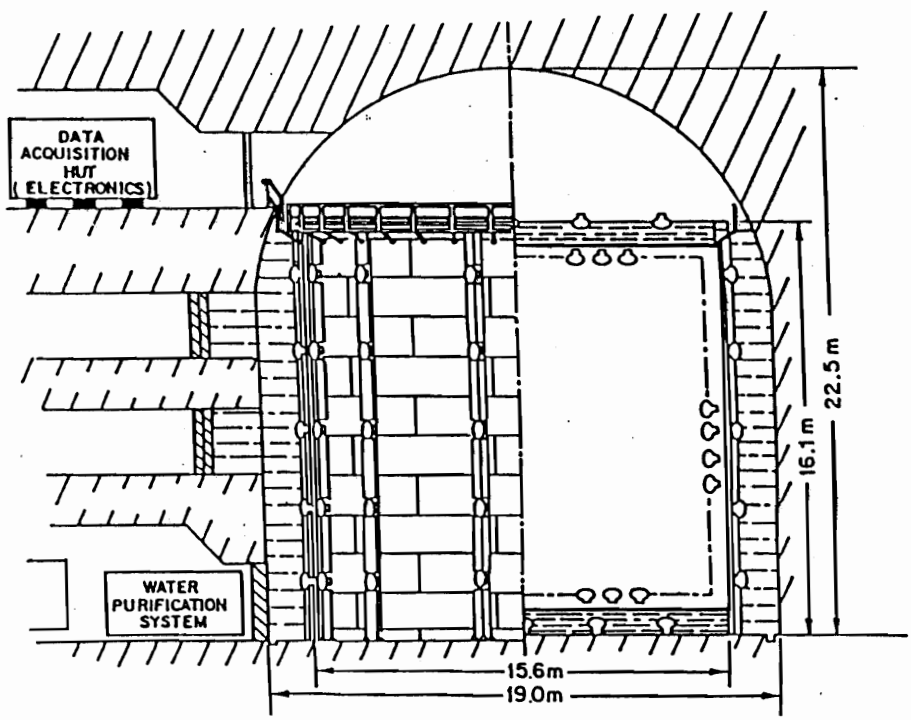

Figure 1:
Schematic drawing of the Kamiokande-II-III detector. The location of the water purification system and the electronics room is also shown.

Kamiokande started its operation in 1983. At the very beginning of the detector operation, it was realized that the energy spectrum of decay electrons from cosmic-ray stopping-muons could be measured down to the 10 MeV energy region. This observation implied that it could be possible to detect ^{8}B solar neutrinos which has the maximum energy of 15 MeV. The most serious problem to be overcome before the observation of solar neutrinos was the reduction of backgrounds. This was made possible by constructing the 4π solid-angle anti-counter and improving the water purification system. For more details of the historical account of Kamiokande, see Ref.[1]. After several years of hardware

improvements, Kamiokande succeeded in observing ^{8}B solar neutrinos in 1987, and the first paper on solar neutrinos was published in 1989 [2], confirming the 20-year-old "missing solar neutrino problem".

The original motivation of the Kamiokande experiment was the search for nucleon decay. As yet, it has not been discovered, with only the lower limits on the nucleon lifetime having been determined[3]. In the search for nucleon decay, a significant number of atmospheric neutrino events were observed. In 1988, Kamiokande[4] observed that the number of single-ring μ-like events, which were mostly due to interactions of atmospheric ν_μ and $\overline{\nu}_\mu$ in the detector, showed a significant deficit compared with the corresponding Monte Carlo (MC) prediction based on a calculated atmospheric neutrino flux, while the number of single-ring e-like events was in good agreement with the expected number. Defining $\mu/e \equiv$ (μ-like, 205 $\sim$ 1500 MeV/c)/(e-like, 100 $\sim$ 1330 MeV/c), $(\mu/e)_{Data}/(\mu/e)_{MC} = 0.56^{+0.09}_{-0.08}$(stat.). The data could be explained by neutrino oscillations either between $\nu_\mu \leftrightarrow \nu_e$ or $\nu_\mu \leftrightarrow \nu_\tau$. This result triggered the current interest in atmospheric neutrinos.

In this report, recent results from Kamiokande on solar and atmospheric neutrinos are described. The data published after the lecture (June 1994) are also included.

2 Solar neutrinos

The Sun is an intense source of low-energy ($E_\nu \lesssim 15$MeV) electron neutrinos (ν_e) that are products of the nuclear processes in its higher temperature central region. Solar neutrinos probe the interior of the Sun, unlike the photons emitted from its surface layer. Also, they provide a means of searching for as yet undetected intrinsic properties of neutrinos through the wide range of matter density and the very long distance from the Sun to the earth.

Our knowledge of the Sun is formulated in a quantitative description known as the standard solar model (SSM) [5][6]. The SSM predicts the fluxes and spectra of solar neutrinos, together with many other physical quantities of the Sun. Fig. 2 shows the calculated fluxes of solar neutrinos on earth. The solar core is believed to be in the hydrogen-burning phase, a sequence of nuclear reactions, which converts four hydrogen into a helium nucleus, two positrons and two electron-neutrinos with a release of 26.7 MeV, of which 3% is carried by neutrinos. The SSM predicts that 98.5% of the total solar energy is generated by a series of reactions initiated by the reaction $pp \rightarrow de^+\nu_e$. The other 1.5% is by the CNO cycle. The total neutrino flux on earth is 6.6×10^{10}/cm^2/sec, of them about 90% are due to the pp reactions. The uncertainty in the calculated flux value for these pp neutrinos are less than 2%. Neutrinos from the $^8\mathrm{B} \rightarrow {}^8\mathrm{Be}^* + \mathrm{e}^+ + \nu_e$ reaction (^{8}B solar neutrinos) are of particular interest by virtue of their relatively high energies, up to 15 MeV, although the neutrino flux is 10^{-4} of the total solar-neutrino flux. The uncertainty of the calculated flux of ^{8}B solar neutrinos is 25$\sim$45%, largely because of the uncertainty in the reaction rate of $^7\mathrm{Be} + \mathrm{p} \rightarrow {}^8\mathrm{B} + \gamma$, which is extremely sensitive to the central temperature of the Sun, and to the value of the reaction cross section at low proton kinetic energy.

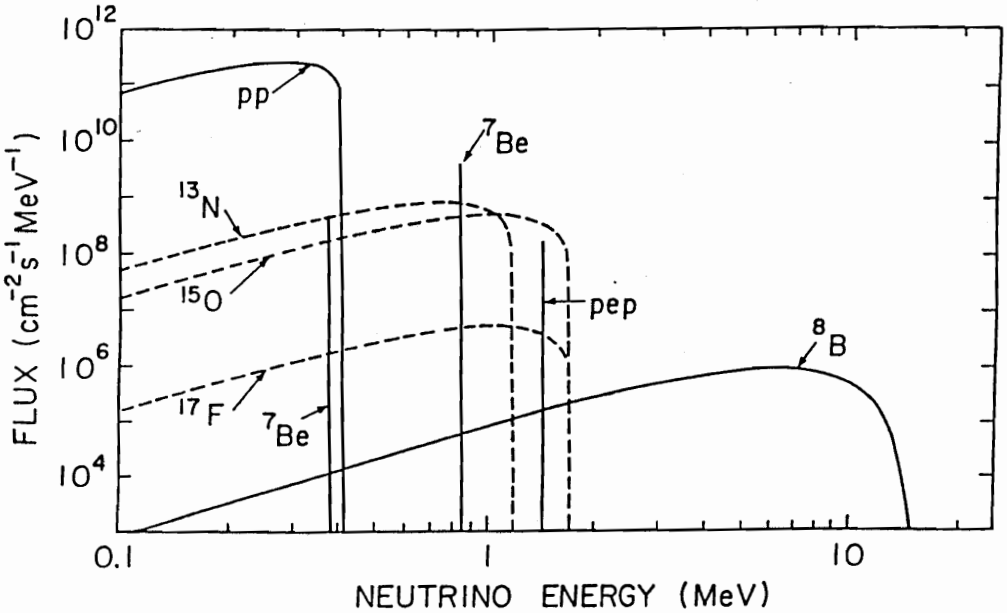

Figure 2:
Calculated fluxes of various solar neutrinos on earth as a function of energy. ^{7}Be and *pep* neutrinos are mono-energetic and their fluxes are in unit of cm^{-2}sec^{-1}.

2.1 Measurement of the ^{8}B solar neutrino flux

Since the beginning of 1986, Kamiokande has been operating with an energy threshold which makes it possible to detect a part of the ^{8}B solar neutrino signal. A history of the trigger and the analysis threshold is schematically shown in Fig. 3. In kamiokande, solar neutrinos are detected through neutrino-electron elastic scattering, $\nu e \rightarrow \nu e$, and the electron energy (E_e), direction and the time of the reaction are measured. The detector has an angular resolution of 28° at 10 MeV, mainly limited by multiple scattering of electrons in the water. The energy resolution for 10 MeV electrons is (at present) 19%. These features make it possible to yield a directional correlation of the solar-neutrino events with respect to the Sun and a measurement of the differential electron energy distribution.

The main backgrounds in the measurement of solar neutrinos in Kamiokande are from natural radioactivity in the detector water, from γ rays emanating from the rock surrounding the detector, and from the β decays of the muon-induced spallation nuclei in the water. At low energies ($\lesssim$7MeV) a significant fraction of the triggered events are due to the β decay of ^{214}Bi(end-point energy=3.26MeV, a daughter of ^{222}Rn). Although the maximum energy of the β spectrum is below the trigger threshold, due to the energy resolution, a fraction (10^{-4} to 10^{-5}) of events are observed as $E_e \sim$7MeV. This background source essentially determines the energy threshold of the analysis. The flux of external γ rays from the surrounding rock is reduced by the anti-counter layer by $\sim$3 orders of magnitude. Most of the remaining γ rays have vertex positions near the surface of the inner-detector, and they are reduced (by more than 2 orders of magnitude) by limiting the fiducial volume to the central 680 tons and by further removing remaining γ rays using information of the reconstructed vertex position and direction. Cosmic-ray muons

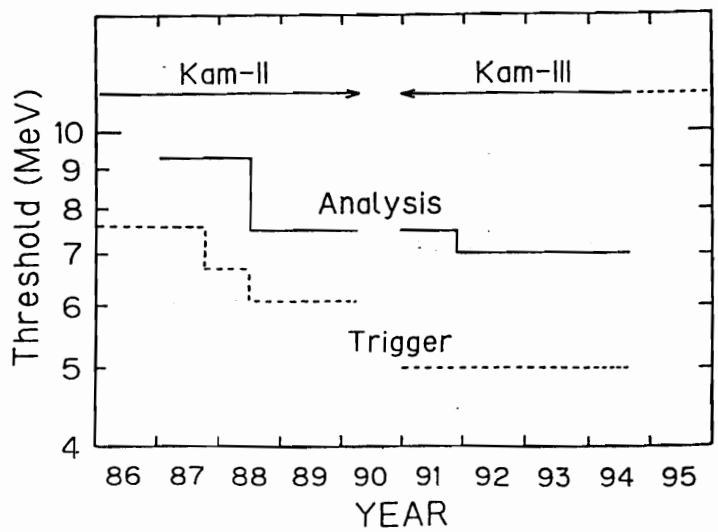

Figure 3:
History of the trigger threshold (dot) of the Kamiokande-II-III detector and the analysis threshold for the solar neutrinos (solid).

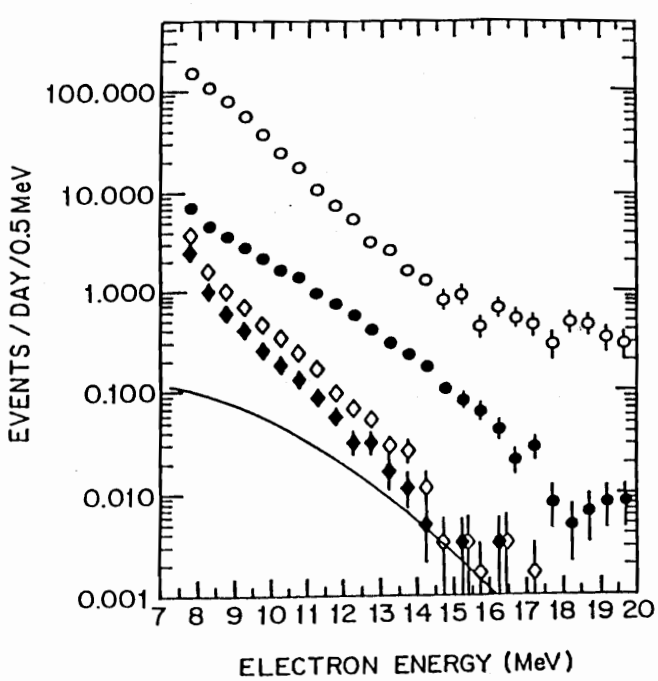

Figure 4:
Event rate as a function of electron energy (E_e) for all events(o), events in the fiducial volume(•), events after spallation cut(◇) and events after the remaining γ-ray cut(◆). The data are from the later stage of Kamiokande-II. The curve shows the expected event rate for the solar neutrinos after all the cuts.

occasionally interact in the detector water and produce radioactive nuclei. These nuclei have typical lifetime of a few tens of milliseconds to several seconds and decay emitting O(10 MeV) β rays. The event rate of such β rays is observed to be ~20 events/day/680tons (>7.5MeV) in Kamiokande. Most of these nuclei are produced along the track of muons. Furthermore, the preceding muons are usually accompanied by an energetic nuclear or electromagnetic shower. Using these characteristics, this background can be reduced by a factor of ~20 (spallation cut). See Ref. [7] for details of the background reduction. Finally, it should be mentioned that all the backgrounds described above have isotropic angular distributions with respect to the direction of the Sun. Taking into account the directional information, the signal and the background are separated statistically. Fig. 4 shows the event rate for each step of the background reduction.

To extract the ^{8}B solar neutrino signal, the event sample after all the cuts was tested for a directional correlation with respect to the Sun. This test provides an additional order of magnitude discrimination against the isotropic background. Fig. 5 shows the distribution in $\cos\theta_\odot$ for the 5.4-year data sample from Kam-II+III. $\cos\theta_\odot$ =1 corresponds to the direction from the Sun to the earth. The solid histogram in the figure shows the shape and the rate of the signal expected from the Monte Carlo simulation based on the SSM of Bahcall and Pinsonneault[5]. The dotted histogram shows the best fit to the data.

Fig. 6 shows the observed energy spectrum of electrons. The solid histogram in the figure shows the shape and the rate of the signal expected from the Monte Carlo simulation based on the $\nu e \rightarrow \nu e$ reaction and the SSM of Bahcall and Pinsonneault [5]. The best-fit spectrum is shown by a dotted histogram and yields 0.48×SSM [5].

The measured flux value for the 5.4-year data sample from Kam-II+III is[2];

$$\frac{Data}{SSM} = 0.48 \pm 0.03(stat.) \pm 0.06(syst.) \qquad \text{(SSM : Bahcall and Pinsonneault[5])},$$

or

$$\frac{Data}{SSM} = 0.62 \pm 0.04(stat.) \pm 0.08(syst.) \qquad \text{(SSM : Turck} - \text{Chieze and Lopes[6])}.$$

The main sources of the systematic error in the flux measurement are uncertainties in absolute energy calibration, in angular resolution, in the calculated dead time of various cuts, and in the possible anisotropy in the $\cos\theta_\odot$ distribution of the background events. The quadratic sum of the uncertainties mentioned above is ±14 and ±12% of the observed signal value in Kam-II and -III, respectively.

2.2 Results from solar neutrino experiments and their implications on neutrino oscillations

We compare the Kamiokande results with those from other solar-neutrino experiments. At present, there are four experiments observing solar neutrinos. The Homestake ^{37}Cl[8] experiment is the first to measure solar neutrinos. This experiment is most sensitive to

[2]All the solar neutrino data from Kam-III are still preliminary.

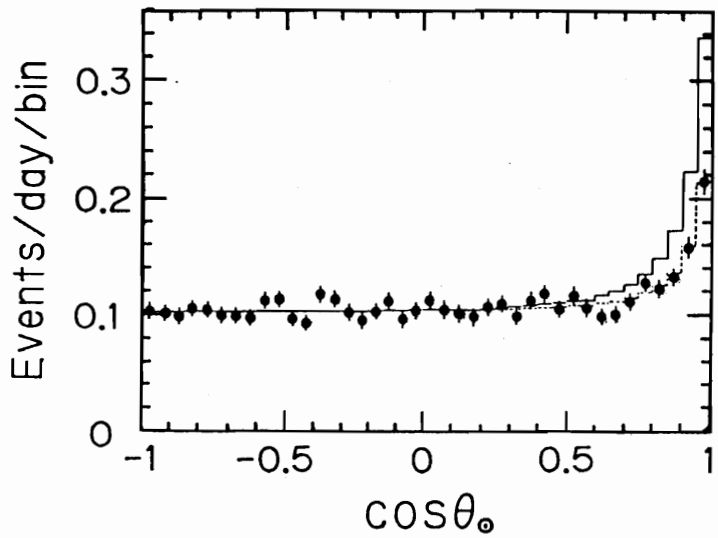

Figure 5:
Plot of the cosine of the angle between the reconstructed electron direction and the direction from the Sun to the earth. The data are for the 5.4-year sample from Kam-II+III. The data could be sub-divided into three based on the analysis threshold; the 1.2-, 2.2- and 2.0-year sample with the analysis threshold of 9.3 MeV, 7.5 MeV and 7.0 MeV, respectively.

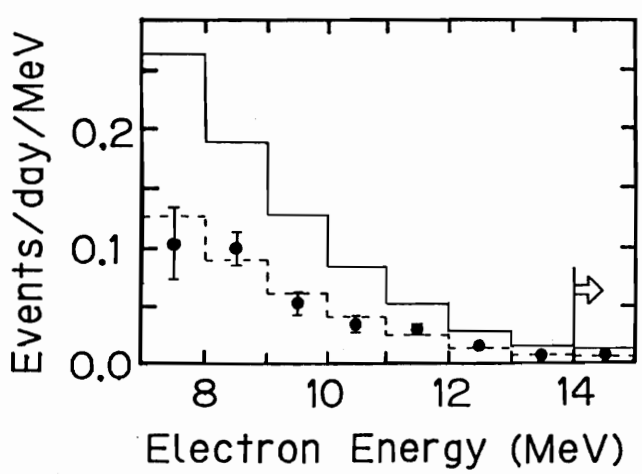

Figure 6:
Differential electron energy distribution of the observed solar-neutrino events. The point above 14 MeV is the sum of all events above 14 MeV.

Table 1:
Experimental results[8][10][9] and the SSM predictions on the solar neutrino flux. Here the unit is SNU for ^{37}Cl and ^{72}Ga and $\nu/\mathrm{cm}^2/\mathrm{sec}$ for $e^-(H_2O)$ target, respectively, where SUN means "solar neutrino unit" defined by 1SNU=$10^{-36}\nu$ captures per atom per second.

(1) SSM=Bahcall and Pinsonneault(*)

Target(Exp.)	Data	SSM prediction	Data/SSM
^{37}Cl(Homestake)	2.28±0.23	8.0±3.0	0.29±0.03
^{71}Ga(SAGE)	73^{+18+5}_{-16-7}	131.5^{+21}_{-17}	$0.56^{+0.14+0.04}_{-0.12-0.05}$
^{71}Ga(Gallex)	79±10±6	131.5^{+21}_{-17}	0.60±0.08±0.05
$e^-(H_2O$, Kamiokande)	$(2.7\pm0.2\pm0.3)\times10^6$	$(5.7\pm2.5)\times10^6$	0.48±0.03±0.06

(2) SSM=Turck-Chieze and Lopes(*)

Target(Exp.)	Data	SSM prediction	Data/SSM
^{37}Cl(Homestake)	2.28±0.23	6.4±1.4	0.36±0.04
^{71}Ga(SAGE)	73^{+18+5}_{-16-7}	123±7	$0.59^{+0.15+0.04}_{-0.13-0.06}$
^{71}Ga(Gallex)	79±10±6	123±7	0.64±0.08±0.05
$e^-(H_2O$, Kamiokande)	$(2.7\pm0.2\pm0.3)\times10^6$	$(4.4\pm1.1)\times10^6$	0.62±0.04±0.08

(*)The uncertainties in the SSM predictions of Bahcall and Pinsonneault [5] represent "total theoretical ranges" or "effective 3σ" as the authors quote. They used 3σ errors for measured quantities. On the other hand, Turck-Chieze and Lopes [6] used 1σ errors for measured quantities in estimating the uncertainties in their SSM calculation.

^{8}B solar neutrinos and is also sensitive to lower energy ^{7}Be solar neutrinos. There are two experiments which use ^{71}Ga as a target, the Gallex[10] experiment in Europe and the SAGE[9] experiment in Russia. A remarkable feature of these experiments is the high sensitivity to the primary *pp* solar neutrinos. Fig. 7 shows the fractional sensitivity of ^{71}Ga, ^{37}Cl and H_2O(Kamiokande) on various solar neutrinos. Table 1 summarizes the results from the four solar neutrino experiments. This table also lists the prediction of the SSM calculations.

It is a quite distinctive feature that all of the results from the present solar neutrino experiments concerning the average flux are less than the SSM predictions. It should also be noted that the observed (Data/SSM) value by the Homestake ^{37}Cl experiment, 0.29±0.04 where SSM by Bahcall and Pinsonneault is used, is significantly smaller than the other results. The other experiments observed the (Data/SSM) value ranging 0.5~0.6. The Kamiokande result on the flux of the ^{8}B solar neutrinos and the Homestake result (mainly) on the ^{8}B and ^{7}Be solar neutrinos suggest that the flux of ^{7}Be solar ν_e should be very small compared with the SSM prediction. This observation makes it extremely difficult to consistently explain in the context of solar physics [11]. The constraints on the fluxes of ^{8}B and ^{7}Be solar neutrinos, together with the results from Ga experiments suggest that the flux of the *pp* solar neutrinos might not be reduced significantly compared

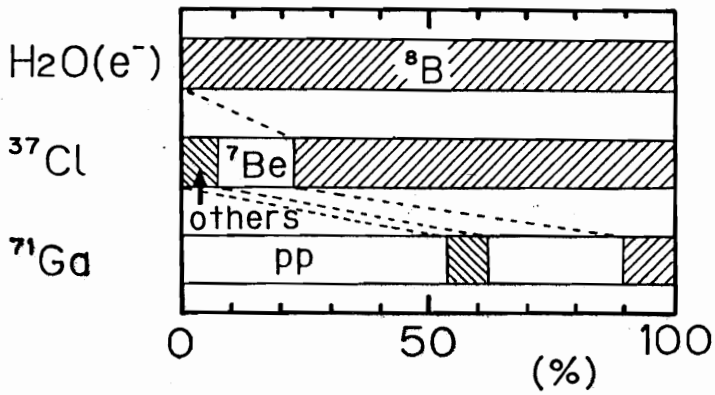

Figure 7:
Fractional sensitivity of H_2O(Target=e^-, Kamiokande), ^{37}Cl and ^{71}Ga on various solar neutrinos. Here the SSM of Bahcall and Pinsonneault [5] is used. 'others' represents *pep*, ^{13}N and ^{15}O solar neutrinos.

with the SSM calculation.

The MSW[12] mechanism is very attractive for explaining all of the existing experimental data. Fig. 8, taken from Ref. [13], shows the 95% C.L. allowed regions in the neutrino-oscillation parameter space. There are two allowed regions, the so-called 'non-adiabatic solution' and 'large-mixing solution'. According to Ref. [13], the data are fit well for the 'non-adiabatic solution'. Although the 'large-angle solution' are allowed at 95% C.L., the goodness of the fit is marginal. Fig. 9 shows the probability of $\nu_e \rightarrow \nu_e$ for two sets of Δm^2 and $\sin^2 2\theta$. These two sets are selected from the allowed regions in Fig. 8. One sees, for the case of 'non-adiabatic solution', that the expected flux of ^{7}Be solar ν_e is very small, the flux of the ^{8}B solar ν_e is reduced to approximately 1/2 of the original value, and the flux of the *pp* solar ν_e is not reduced significantly. This is what is suggested by the above discussion combining all the solar neutrino data.

2.3 Energy spectrum and day-night data

So far, we observed that the MSW mechanism might be an attractive solution to the solar neutrino problem. Fig. 9 suggests that the spectrum of the ^{8}B solar neutrinos could be distorted for the case of the 'non-adiabatic solution', or the day-night effect should be observed for the case of the 'large-angle solution'. Kamiokande data have information for both the energy spectrum and the day-night effect. Fig. 10 shows the Kamiokande data on the energy spectrum of the recoil electrons from νe scattering at $E_e \geq 7$ MeV. Also shown are the expected spectrum for 'non-adiabatic solution' and 0.48×SSM. The accuracy of the present data can not distinguish between the two cases.

Fig. 11 shows the Kamiokande day-night data. The data indicate no statistically significant flux difference between day and night. Specifically, the relative flux difference between the day-time and night-time is expressed by

$$\frac{day - night}{day + night} = -0.07 \pm 0.07(\text{stat.}).$$

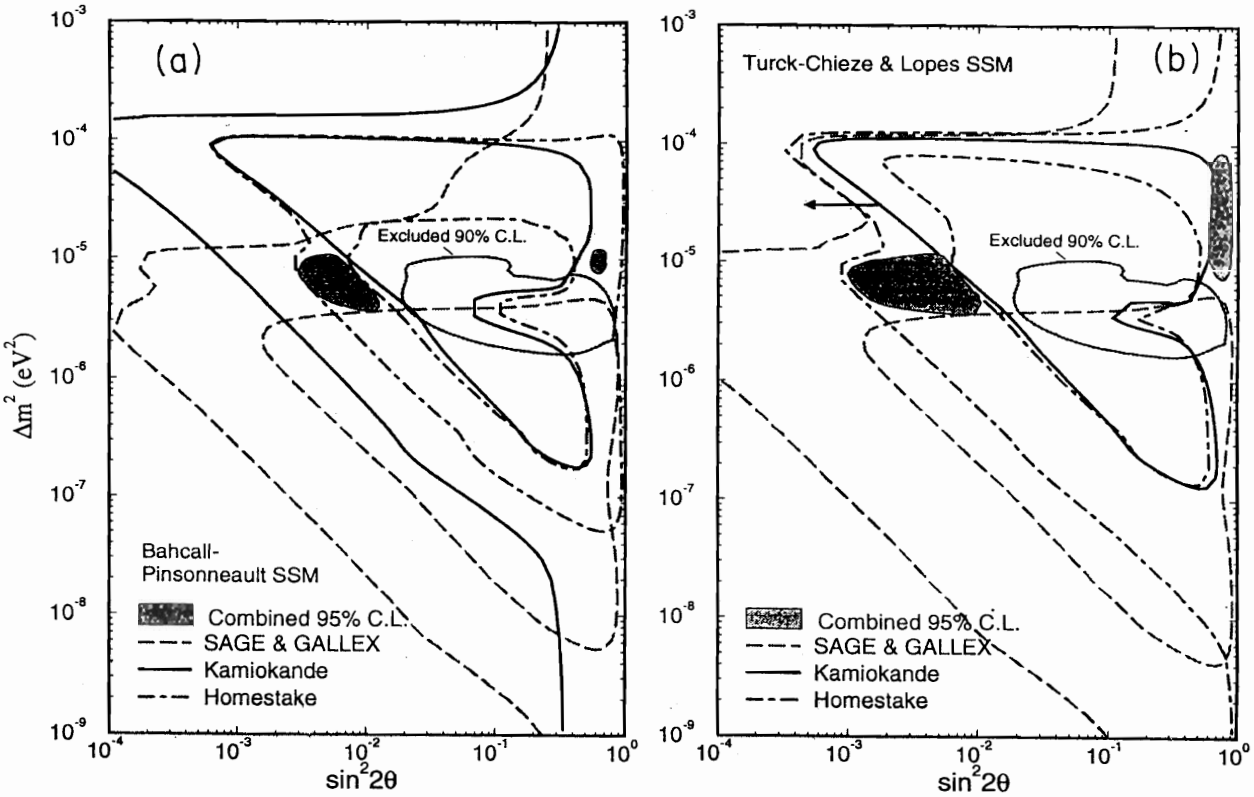

Figure 8:

The allowed parameter regions of the Homestake, Kamiokande, and Ga experiments, and the combined data. Here SSM's are (a) by Bahcall & Pinsonneault and (b) by Turck-Chieze & Lopes. The SSM uncertainties are included in the analysis. These figures are taken from Ref. [13]. For the Bahcall & Pinsonneault SSM, the 1σ value of the SSM uncertainties is assumed to be 1/3 of their 'effective 3σ error'. The earth effect on the regeneration of ν_e is included. The excluded region by the Kamiokande day/night data[14] are also shown.

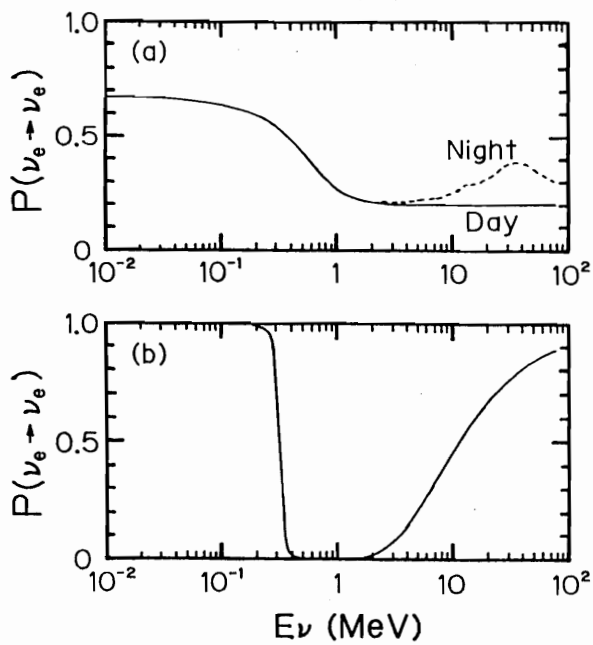

Figure 9:

The probability that a solar ν_e remain ν_e for (a) $(\Delta m^2, \sin^2 2\theta)=(1\times10^{-5}, 0.6)$, i.e., the large-angle solution, and (b) $(\Delta m^2, \sin^2 2\theta)=(0.5\times10^{-5}, 0.6\times10^{-2})$, i.e., the non-adiabatic solution. In (a), the flux of ν_e for both day and night are shown. In (b), the flux difference between day and night is negligible.

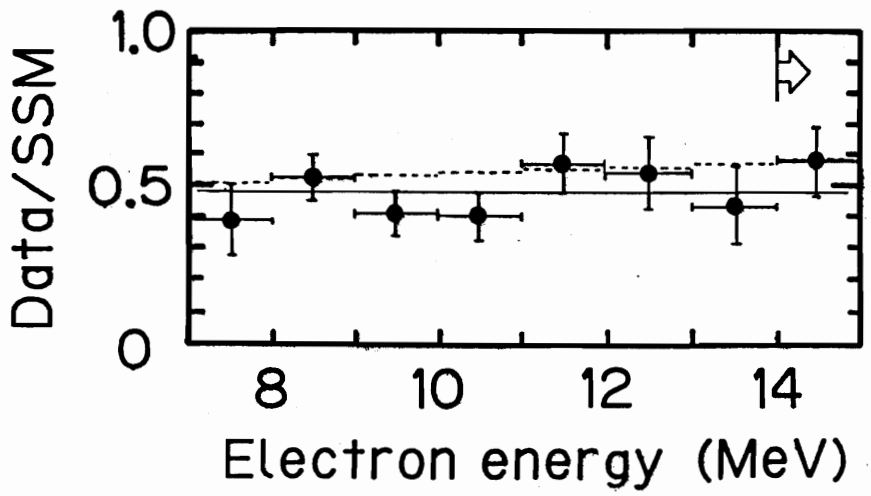

Figure 10:
Data/SSM[5] as a function of electron energy. Also shown are the expected spectrum for 'non-adiabatic solution', i.e., (Δm^2, $\sin^2 2\theta$)=(0.5×10^{-5}, $0.6\times10-2$) (dot), and $0.48\times$SSM (solid).

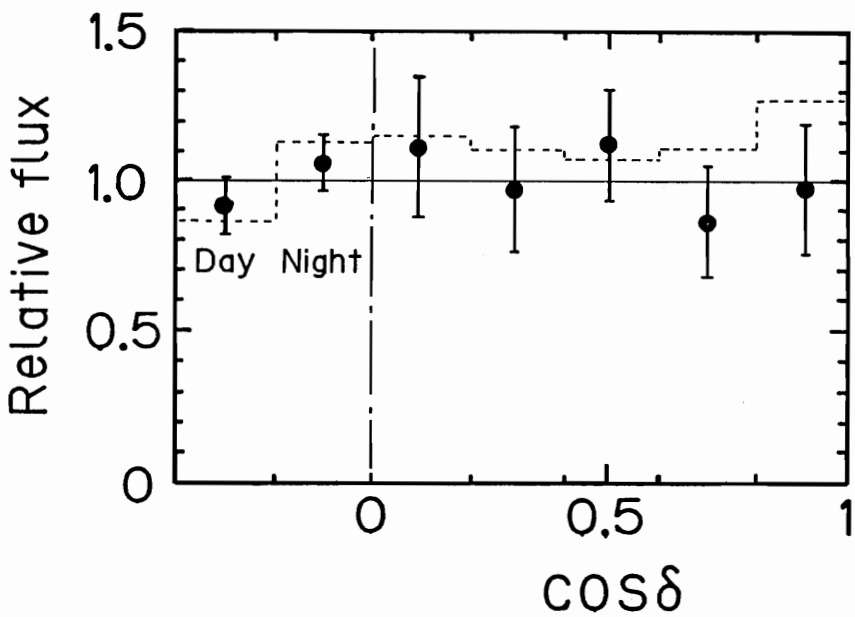

Figure 11:
Kamiokande day-night data are shown. Here the y-axis is normalized so that the observed flux averaging day and night is 1. The night-time data are shown with five bins according to the angle between the direction to the Sun and the nadir at the detector. ($\cos\delta$=1 corresponds to upward-going neutrinos.) Also shown by dotted histogram is the expected day-night flux difference for 'large angle solution', i.e., (Δm^2, $\sin^2 2\theta$) = (1×10^{-5}, 0.6).

2.4 Future prospect

In the above discussion, we observed that the MSW mechanism could explain the present solar neutrino data well. However, it should be noted that the above discussion and the resultant allowed parameter regions of neutrino oscillations rely heavily on all the experiment. If one ignores one of the the three results, i.e., one of Kamiokande, Homestake and (SAGE+Gallex), the allowed regions get much bigger, see Fig 8. Much stronger evidence for the MSW effect might be necessary before fully settling the 'solar neutrino problem'.

The present data and the MSW solution have several predictions to be observed in future solar neutrino experiments. They are:
(1) The flux of ^{7}Be solar ν_e should be much lower than the SSM prediction.
(2) And, the energy spectrum of ^{8}B solar neutrinos should be distorted.
(3) Or, there should be a difference in the flux between day-time and night-time.
Kamiokande have searched for any evidence for (2) or (3), but no statistically significant effect has been observed. Future solar neutrino experiments such as SNO [15] or Super-Kamiokande [16] are sensitive to (2) and (3). BOREXINO [17] is aiming at detecting ^{7}Be solar neutrinos and a very important test for (1) could be made.

SNO is a 1000 ton heavy water Cerenkov detector designed to study the intensity and energy of ^{8}B solar neutrinos. The unique feature is the use of heavy water (D_2O) which enables both electron neutrinos and all types of neutrinos to be measured by the reactions; (a) $\nu_e + d \rightarrow e^- + p + p$, and (b) $\nu_x + d \rightarrow \nu_x + p + n$(neutrons are detected as a signature of ν_x interaction.). Since the reaction (b) is equally sensitive to all neutrinos, it would be used to measure the total flux of ^{8}B solar neutrinos independent of neutrino oscillations. The reaction (a) is useful for measuring the energy spectrum of ^{8}B solar neutrinos.

BOREXINO is a liquid-scintillator detector. It detects the scintillation light from electrons produced by the reaction $\nu_x + e^- \rightarrow \nu_x + e^-$. The use of liquid-scintillator with low-radioactive contamination would enable the detection of ^{7}Be solar neutrinos with a tolerable background contamination.

SNO and Super-Kamiokande will start its experiment in 1995 and 1996, respectively. In the next few years, these experiments should be able to constrain the parameter space precisely and check the consistency of the MSW predictions.

3 Atmospheric neutrinos

Atmospheric neutrinos arise from the decay of secondaries (π, K and μ) produced by primary cosmic-ray interactions in the atmosphere. In the energy range below $E_\nu \sim 1$ GeV, where all secondaries decay, we roughly expect that $(\nu_\mu+\overline{\nu}_\mu)/(\nu_e+\overline{\nu}_e)\simeq 2$. This is because a π-decay produces a ν_μ and a μ; the μ, when it decays, produces another ν_μ and a ν_e. These neutrinos enter into the detector from all directions nearly isotropically. In the energy range above $E_\nu \sim 1$ GeV, a fraction of muons do not decay before reaching the ground. Accordingly, the $(\nu_\mu+\overline{\nu}_\mu)/(\nu_e+\overline{\nu}_e)$ ratio increases as increasing E_ν, see Fig. 12. As seen from Fig. 12, the agreement of the $(\nu_\mu+\overline{\nu}_\mu)/(\nu_e+\overline{\nu}_e)$ ratio between independent flux calculations is better than 5%. Also, since the probability of these muons hitting

Table 2:
Summary of the basic numbers for the analysis of atmospheric neutrinos in Kamiokande. Sub-GeV data are from Kam-I+II+III, multi-GeV data are from Kam-II+III and upward-going muon data are from Kam-I+II.

	sub-GeV	multi-GeV fully-contained	multi-GeV partially-contained	up-going μ
$<E_\nu>$	~0.7 GeV	~6 GeV		~100 GeV
Fiducial mass	1.04 kt(*)	1.35 kt	1.04 kt	—
Total exposure	7.7 kt·yr	8.2 kt·yr	6.0 kt·yr	4.0+1.2(**)yr
Number of ev.	690	195	118	252
		313		

(*) 0.88 (and 0.78) kton in Kam-I.
(**) The 1.2 yr data are not fully efficient because of an on-line selection.

the ground before their decay depends on zenith-angle, there is a zenith-angle dependence of the neutrino flux in the multi-GeV energy range, see Fig. 13. The path length of the neutrinos (from the production point to the detector) ranges from a few km to 13000km, the diameter of the earth.

In this chapter, I would like to describe the recent measurements of the atmospheric neutrinos from Kamiokande and compare them with those from other large underground detectors. Some of the experiments observed that the $(\nu_\mu+\overline{\nu}_\mu)/(\nu_e+\overline{\nu}_e)$ ratio is significantly smaller than expected. The interpretation of these interesting results, the future prospect on atmospheric neutrino observations and the related neutrino physics are also described. In most parts of this chapter, when mention is made of neutrinos, we imply both neutrinos and anti-neutrinos.

In the following sub-sections, I would like to describe the 'sub-GeV' and 'multi-GeV' data whose mean energies of neutrinos are about 0.7 and 6 GeV. respectively. Also, I would like to comment on the upward-going muon data briefly. Some of the basic numbers related to the atmospheric-neutrino analysis are summarized in Table 2.

3.1 Sub-GeV data

The main aim of the Kamiokande experiment when it started taking data was the search for nucleon decay. In order to search for these events, fully-contained events whose vertex positions were in the fiducial volume and no visible track exiting from the inner detector were selected. Since nucleon decay signals should have visible energy (E_{vis}) less than 1 GeV, the energy range covered in this series of analysis was $30<E_{vis}<1330$ MeV, corresponding to 30 to 1330 MeV/c for electrons and 205 to 1500 MeV/c for muons. In the course of the analysis, a significant number of atmospheric neutrino events were observed, ~100 events per kton·yr of the detector exposure. The mean energy of neutrinos for such events with single Cerenkov-ring topology is about 700 MeV. We call these events as 'sub-GeV' data.

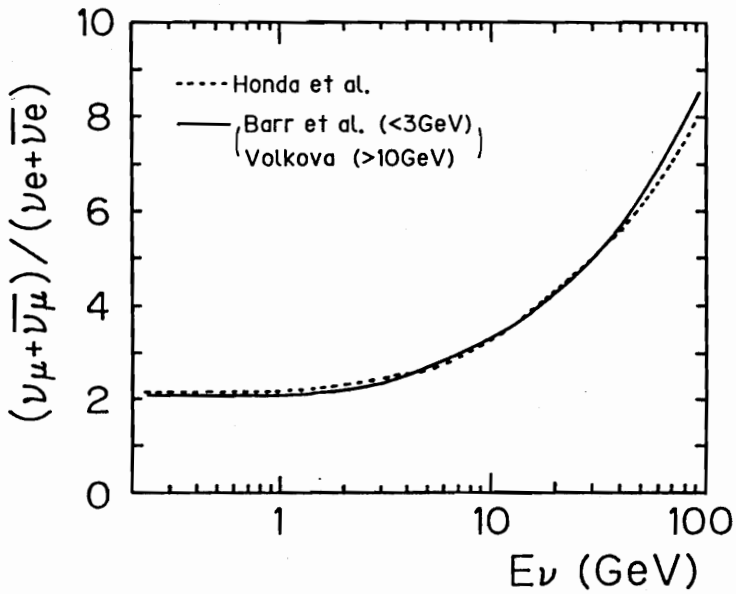

Figure 12:
Calculated $(\nu_\mu+\overline{\nu}_\mu)/(\nu_e+\overline{\nu}_e)$ flux ratio as a function of neutrino energy by several flux calculations. The solid curve is drawn using the calculated flux by Barr et al., [20] for E_ν <3 GeV and by Volkova [24] for E_ν >10 GeV and smoothly connecting the two fluxes at 3<E_ν <10 GeV.

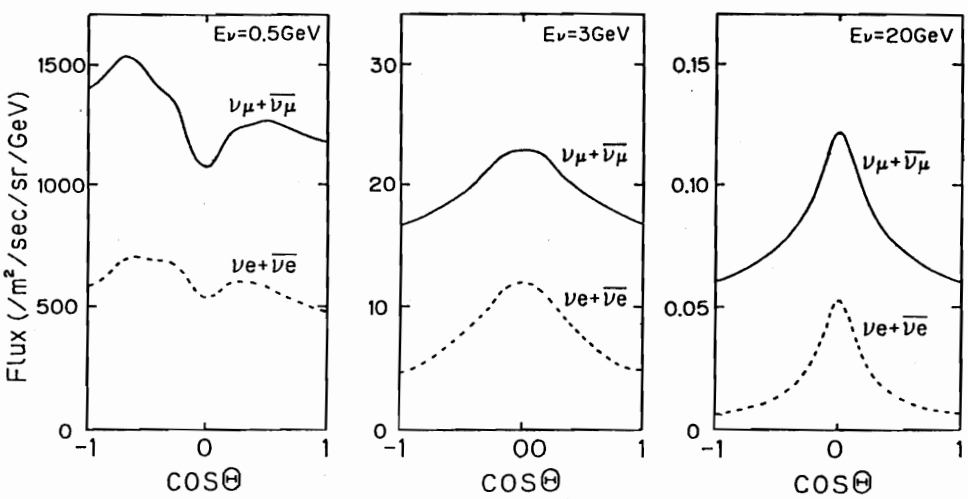

Figure 13:
Zenith-angle dependence of the calculated $(\nu_\mu+\overline{\nu}_\mu)$ and $(\nu_e+\overline{\nu}_e)$ fluxes for several neutrino energies (Honda et al., [21]). An apparent suppression of the fluxes at around cosΘ =0 (horizontal) for E_ν =0.5 GeV is due to the east/west effect (i.e., the suppression of cosmic ray fluxes arriving from east due to the geomagnetic cutoff). The relative suppression of downward-going neutrinos for E_ν =0.5 GeV is also due to the geomagnetic-cutoff effect, (i.e., relatively strong geomagnetic field at the Kamioka site (26°N geomagnetic latitude)). The geomagnetic-cutoff effect is small for multi-GeV neutrinos.

During 7.7kt·yr of the detector exposure, Kamiokande observed 690 such atmospheric neutrino interactions. Among them, 482 had single Cerenkov-ring topology. For the analysis of the atmospheric ν_μ/ν_e ratio, only single-ring events are used. This is because (i) the fraction of neutral current events (i.e., the background events for the measurement of the ν_μ/ν_e ratio) in the single- and multi-ring events are estimated to be 4 and 38%, respectively; and (ii) in the low-energy multi-ring events, it is not easy to select a ring due to a lepton among the observed Cerenkov rings.

Muons and electrons, which are respectively produced by the interactions of ν_μ and ν_e, are separated by a particle identification program. The particle identification program makes use of the spatial distribution of photoelectrons. Electrons, due to electromagnetic showers and multiple scattering of low-energy electrons, produce more diffuse Cerenkov rings than those produced by muons. The reconstructed opening angle of the Cerenkov cone is additionally used, because β =1 and <1 for electrons and muons, respectively. The probability of misidentifying the particle species of single-ring events was estimated to be 2% using Monte Carlo simulated neutrino events. The method was checked by means of cosmic-ray stopping-muons entering the Kamiokande detector. The analysis of stopping muons showed that the misidentification probability of muons was 2%.

The particle identification was also checked by a beam test in which the beam from an accelerator was exposed to a 1000-ton water Cerenkov detector at KEK. The preliminary result [18] shows that the identification probability for real electrons and muons is as good as expected by the Monte Carlo simulation. Accordingly it is unlikely that the particle identification program gives substantially incorrect assignments to the real fully contained events observed in Kamiokande.

To understand the fully contained events qualitatively, a Monte Carlo program is used to simulate the atmospheric neutrino interactions in the detector[19]. It uses the atmospheric neutrino fluxes calculated for the Kamioka site[20][21][22][23]. Data on neutrino cross sections and kinematics are taken from low energy neutrino experiments at ANL, BNL and CERN. The processes considered include quasi-elastic scattering, single-pion production and multi-pion production from both charged and neutral currents (CC and NC). Various nuclear effects are taken into account. Then the simulated events are passed through the same analysis procedure as the data.

Table 3 summarizes the data and compares them with the Monte Carlo estimations. A total of 234 μ-events and 248 e-events were observed. We show four Monte Carlo predictions in an effort to treat the flux calculations symmetrically. We emphasize that the ratio $(\mu/\mathrm{e})_{data}/(\mu/\mathrm{e})_{MC}$ is essentially independent of the calculated absolute values of the ν_μ and ν_e fluxes as shown in Table 3. Hereafter, for simplicity, we use the flux calculated by Honda et al. [21]. $(\mu/\mathrm{e})_{data}/(\mu/\mathrm{e})_{MC}$ =$0.60^{+0.06}_{-0.05}$(stat).

We discuss the systematic errors involved in the flux calculations, the measurements and the MC predictions. Table 4 summarizes the possible sources of the systematic error in the $(\mu/\mathrm{e})_{data}/(\mu/\mathrm{e})_{MC}$ ratio. Adding all the errors in quadrature, systematic error in $(\mu/\mathrm{e})_{data}$ / $(\mu/\mathrm{e})_{MC}$ is estimated to be 9%. Then $(\mu/\mathrm{e})_{data}$ / $(\mu/\mathrm{e})_{MC}$ of the Kamiokande sub-GeV data is;

$$(\mu/e)_{data}/(\mu/e)_{MC} = 0.60^{+0.06}_{-0.05}(stat) \pm 0.05(syst).$$

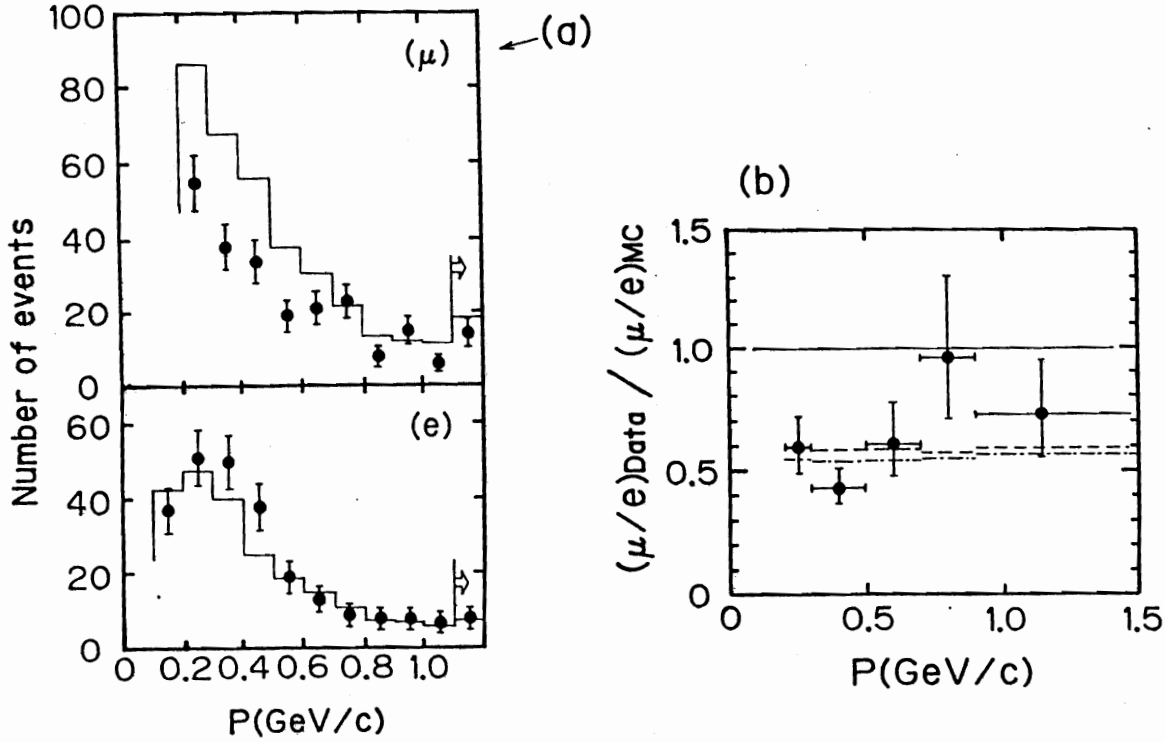

Figure 14:
(a) The momentum spectra of e- and μ-events. The histograms show the Monte Carlo prediction based on the flux calculation by Honda et al. (b) The momentum dependence of $(\mu/e)_{data}/(\mu/e)_{MC}$. The MC predictions with neutrino oscillations $((\Delta m^2_{\nu_\mu\nu_e}, \sin^2 2\theta_{\nu_\mu\nu_e}) = (2.2\times10^{-2}\mathrm{eV}^2, 0.75)$ (dash, the best-fit parameter set for the sub-GeV data) and $(\Delta m^2_{\nu_\mu\nu_e}, \sin^2 2\theta_{\nu_\mu\nu_e}) = (1.6\times10^{-2}\mathrm{eV}^2, 0.98)$ (dash-dot, the best-fit parameter set for the Kamiokande sub+multi-GeV data) are shown by histograms.

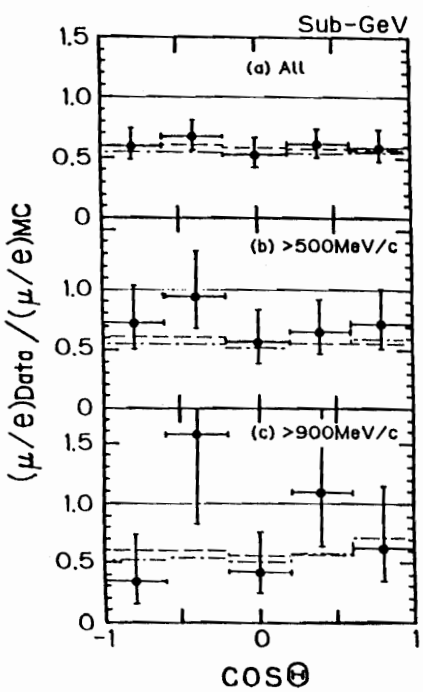

Figure 15:
Zenith-angle dependence of $(\mu/e)_{data}/(\mu/e)_{MC}$ for (a) the full sub-GeV data and the sub-GeV data with the minimum momentum cuts at (b) 500 MeV/c and (c) 900 MeV/c. The MC predictions with neutrino oscillations $((\Delta m^2_{\nu_\mu\nu_e}, \sin^2 2\theta_{\nu_\mu\nu_e}) = (2.2\times10^{-2}\mathrm{eV}^2, 0.75)$ (dash, the best-fit parameter set for the sub-GeV data) and $(\Delta m^2_{\nu_\mu\nu_e}, \sin^2 2\theta_{\nu_\mu\nu_e}) = (1.6\times10^{-2}\mathrm{eV}^2, 0.98)$ (dash-dot, the best-fit parameter set for the Kamiokande sub+multi-GeV data) are shown by histograms.

Table 3:
Summary of the sub-GeV atmospheric neutrino data from Kam-I-II-III. The detector exposure is 7.7 kton·yr.

Type of ev.	Data	νMC(*)			
		Honda et al.	Barr et al.	Lee et al.(**)	Bugaev et al.
Single ring(***)	482	584.3	653.2	511.5	431.9
μ-like	234	356.8	396.0	312.2	263.8
e-like	248	227.6	257.2	199.3	168.1
Multi ring	208	233.8	253.8	200.0	193.6
Total ev.	690	818.1	907.0	711.5	625.4
$(\mu/e)_{data}/(\mu/e)_{MC}$ $\Longrightarrow$		$0.60^{+0.06}_{-0.05}$	$0.61^{+0.06}_{-0.05}$	$0.60^{+0.06}_{-0.05}$	$0.60^{+0.06}_{-0.05}$

*) Each Monte Carlo prediction is based on 43kt·yr equivalent simulated data. The Monte Carlo events are passed through the same analysis chain.
**) It should be commented that this flux predicts $\nu_e/\overline{\nu}_e$ ratio to be unity, while the expected value is ~1.2 as expected from the observed μ^+/μ^- flux ratio. Thus one should make corrections of the $\nu_e/\overline{\nu}_e$ ratio for more precise arguments.
***) $0.1 < p_e < 1.33$ GeV/c for the e-like events and $0.2 < p_\mu < 1.5$ GeV/c for the μ-like events.

The relative deficit of the μ-like events of the data can be tested by studying the number of events followed by μ-decay signals. A large fraction of CC ν_μ induced single-ring events are accompanied by μ-decay electrons, while most of CC ν_e induced single-ring events are not. Therefore a ratio $R_{decay} \equiv$ (single-ring events with μ decay) / (single-ring events without μ decay) is related to the ν_μ/ν_e ratio. The data on the events with μ-decay is summarized in Table 5. Data/MC of R_{decay} is; $R_{decay}(\text{Data})/R_{decay}(\text{MC}) = 0.70^{+0.07}_{-0.06}(\text{stat.})$, in reasonable agreement with the value obtained from the particle identification. It is also important that, as shown in Table 5, the expected and observed μ-decay fraction agrees well for both e- and μ-like events.

Finally, the momentum spectra of the events and the momentum dependence of $(\mu/e)_{data}/(\mu/e)_{MC}$ are shown in Fig. 14. The zenith-angle dependence of $(\mu/e)_{data}/(\mu/e)_{MC}$ is shown in Fig. 15. One finds that $(\mu/e)_{data}/(\mu/e)_{MC}$ does not show any strong momentum and zenith-angle dependences in this energy range.

3.2 Multi-GeV data

In the previous subsection, fully-contained events with visible-energy (E_{vis}) lower than 1.33 GeV (sub-GeV data) were described. Here we present the data from atmospheric-neutrino interactions in the 'multi-GeV' energy range in the Kam-II-III detector. They are (i) fully-contained events with E_{vis} higher than 1.33 GeV, and (ii) partially-contained events which have their interaction vertex in the fiducial volume and at least one visible track exiting from the inner-detector. These data constitute a completely independent data sample from the one described in the previous subsection, i.e., there is no overlap of events between these two samples.

Table 4:

Sources of systematic error in $(\mu/e)_{data}/(\mu/e)_{MC}$ for the sub-GeV data.

$(\nu_\mu+\overline{\nu}_\mu)/(\nu_e+\overline{\nu}_e)$	<5%	
$\nu_e/\overline{\nu}_e$	2%	(*)
μ/e separation	4%	(**)
1ring/2ring separation	2%	
Vertex position determination	1%	
Absolute energy calibration	1%	
Non-neutrino background	<1%	
CC cross section	3%	(***)
NC cross section	2%	
γ ray from exited nuclei	1%	
Statistical fluctuation of MC	3.6%	
Total (added in quadrature)	9%	

(*) 8% error in the $\nu_e/\overline{\nu}_e$ flux ratio changes the μ/e ratio by 2%.
(**) Error in the μ/e separation affects the numerator and the denominator in μ/e in opposite directions. Thus the systematic error is 2 times 2% misidentification probability.
(***) The possible sources considered here are uncertainty in; M_A in quasi-elastic interaction, Fermi surface momentum in quasi-elastic interaction with ^{16}O, nuclear potential, $\sigma(\nu_\mu)/\sigma(\nu_e)$ for CC $m\pi(m \geq 1)$ processes, and the absolute cross sections of CC $m\pi(m \geq 1)$.

Table 5:

Fraction of μ-decay for single-ring events.

Type of ev.	Data			Monte Carlo		
	total ev.	μ decay	μ-decay fraction	total ev.	μ decay	μ-decay fraction
Single ring	482	182	0.38±0.03	584.3	270.5	0.46
μ-like	234	158	0.68±0.04	356.8	247.9	0.69
e-like(*)	248	24	0.10±0.02	227.6	22.6	0.10

*) Many of the e-like events with μ-decay signals are from CC single π^+ production of $(\overline{\nu}_e)$. These π^+ have energies below the threshold of Cerenkov radiation and decay to μ^+. Then the decays of the μ^+ are observed.

These multi-GeV data are useful from two points of view. First, the ratio of the number of μ-like to e-like events normalized by the corresponding ratio of the Monte Carlo simulation, $(\mu/e)_{data}/(\mu/e)_{MC}$, provides an independent measurement of that ratio to be compared with the result from the sub-GeV data. Second, valuable information on neutrino oscillations might be extracted by studying the zenith-angle dependence of the μ/e ratio. This is made possible by the large difference of the path-length between downward-going neutrinos ($\lesssim$20 km) and upward-going neutrinos ($\approx 10^4$ km), together with the better angular correlation between the neutrinos and the produced charged-leptons for these multi-GeV neutrinos (r.m.s.=15$\sim$20°) relative to the angular correlation (r.m.s.$\sim$60°) in the sub-GeV range.

We observed 195 fully-contained events with E_{vis} >1.33 GeV during 8.2 kton·yr of the Kam-II-III detector exposure. Of them, all single ring events are subject to particle identification. Then each event is classified as either e- or μ-like. In a multi-ring event, the lepton flavor can be identified if the charged lepton carries a significant fraction of the total visible energy. Thus we use some fraction (about 30%) of the multi-ring events for the study of the μ/e ratio. A Cerenkov ring that contributes more than 80% of the total visible energy is assumed to be due to a lepton and the particle identification is applied to the ring. This procedure successfully selects CC ν_e and ν_μ events. We observed 31 (21 single-ring and 10 multi-ring) such μ-like and 98 (73 single-ring and 25 multi-ring) such e-like events. According to the Monte Carlo events, the purity of CCν_μ and CCν_e in the selected μ-like and e-like events are greater than 95% and 90%, respectively.

We observed 118 partially-contained events during 6.0 kton·yr of the Kam-II-III detector exposure. The detection efficiency of the partially-contained events in the fiducial volume is estimated to be 92% by MC events. Muons that have energy higher than a few GeV cannot be contained in the Kamiokande detector. Accordingly, the partially-contained events are dominated by multi-GeV CC ν_μ interactions. However, there are non-negligible contaminations of CC ν_e and NC events. We make a simple cut to improve the purity of CC ν_μ events in the partially-contained μ-like sample. A single-ring partially-contained event is eliminated if it is identified as e-like, which eliminates about 8% of the partially-contained events. All the multi-ring partially-contained events are taken to be μ-like. 94% of the remaining partially-contained events are estimated to be due to CC ν_μ interactions, and we assign all these events as μ-like. (We do not use the single-ring partially-contained e-like events in the analysis, because the estimated fraction of CC ν_e in this category of events is only 42%.) We observed 104 such partially-contained μ-like events.

To understand these events quantitatively, Monte Carlo simulated events [19] are generated and passed through the same analysis procedure as the data. In this analysis two fluxes are used. One is the flux calculated by Honda et al. [21]. The other is the flux of Ref.[20] for neutrino energy (E_ν) <3 GeV and Ref.[24] for E_ν >10 GeV. For E_ν between 3 and 10 GeV the two fluxes are smoothly connected (Barr et al./Volkova−flux). These calculated fluxes are suitable for the present study, because the flux values for ν_e, $\overline{\nu}_e$, ν_μ and $\overline{\nu}_\mu$ from (lower than) 100 MeV to (higher than) 100 GeV are available, and the muon-polarization effect and the geomagnetic cutoff are taken into account. Table 6 summarizes the data and compares them with the corresponding Monte Carlo simulations,

Table 6:
Summary of the multi-GeV data from Kam-II-III and simulated atmospheric neutrino interactions for two fluxes.

		Data(*)	νMC(**)	
	Flux ⇒		Honda et al	Barr et al./Volkova
Fully-contained(***)	Total	195	181.0	189.1
	e-like	98	66.5	70.8
	μ-like	31	37.8	40.4
Partially-contained(****)	Total	118	135.5	136.6
	e-like	–	–	–
	μ-like	104	124.4	125.4
Total	e-like	98	66.5	70.8
	μ-like	135	162.2	165.8
	$(\mu/e)_{data}/(\mu/e)_{MC}$		$0.57^{+0.08}_{-0.07}$	$0.59^{+0.08}_{-0.07}$

*) The detector exposures are 8.2 kton·yr and 6.0 kton·yr for the fully-contained and partially-contained events, respectively.
**) Each Monte Carlo prediction is based on 51 kton·yr and 40 kton·yr equivalent simulated data for fully-contained and partially-contained events, respectively.
***)E_{vis} >1.33GeV.
****) No E_{vis} cut at 1.33 GeV.

which are seen to be in good agreement with each other.

Figs. 16(a) ~ (c) show the E_{vis} distributions which are informative for understanding the energy range relevant to the present study. Although some of the partially-contained μ-like events appear in the E_{vis} distribution in Fig. 16(c) below 1 GeV, as is predicted by the Monte Carlo simulation, the energy of neutrinos giving rise to these are above 1 GeV. Based on the Monte Carlo simulations, the mean energy of neutrinos is 5 GeV for the fully-contained e-like events, 2.5 GeV for the fully-contained μ-like events, and 9 GeV for the partially-contained μ-like events. If we combine the fully-contained μ-like and partially-contained μ-like events, the mean energy of neutrinos for these μ-like events is 7 GeV. Thus the mean neutrino energies are similar for μ-like and e-like events in these samples. These numbers suggest that the μ/e ratio can be obtained by combining the multi-GeV fully-contained and partially-contained events, i.e., μ/e ≡ (fully-contained μ-like + partially-contained μ-like events)/(fully-contained e-like events). From Table 6, one can calculate:

$$\frac{(\mu/e)_{data}}{(\mu/e)_{MC}} = 0.57^{+0.08}_{-0.07}(\text{stat.}) \pm 0.07(\text{syst.}) \qquad (\text{Flux} = \text{Honda et al.}),$$

which suggests that the atmospheric $(\nu_\mu + \overline{\nu}_\mu)/(\nu_e + \overline{\nu}_e)$ ratio is smaller than expected in the multi-GeV energy range. Table 7 summarizes the systematic error in the μ/e ratio in the multi-GeV data. This result agrees well with that obtained in the sub-GeV.

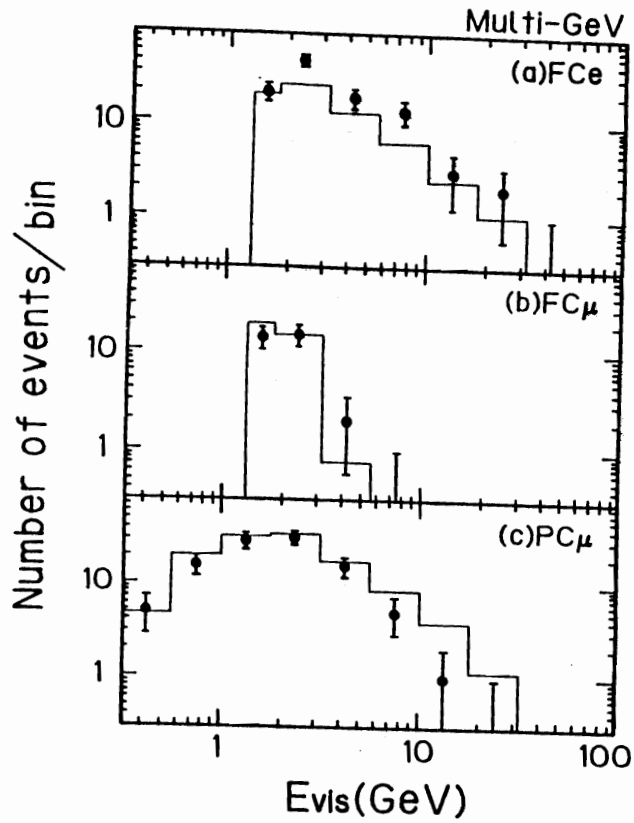

Figure 16:
Visible-energy (E_{vis}) distributions for the (a) fully-contained e-like events, (b) fully-contained μ-like events and (c) partially-contained μ-like events. The circles with error bars show the data and the histogram the MC (without neutrino oscillations).

Fig. 17 shows the zenith-angle distribution for the (a) e-like events, and (b) μ-like events. One sees that the e-like events have a small excess of events for the upward- and horizontal-going directions and the μ-like events have a small deficit of events in the same directions. These non-uniform zenith-angle dependences can more clearly be seen in Fig. 18, which shows the zenith-angle dependence of $(\mu/e)_{data}/(\mu/e)_{MC}$. It should be noted that the systematic error associated with any up/down asymmetry is negligible compared with the statistical error.

The observed zenith-angle distribution of $(\mu/e)_{data}/(\mu/e)_{MC}$ does not seem flat. A statistical analysis suggests that the assumption of the uniform zenith-angle distribution could be excluded at about 99% C.L. A possible explanation of this non-uniform zenith-angle distribution together with the small $(\mu/e)_{data}/(\mu/e)_{MC}$ may be sought in neutrino oscillations. In the next sub-section, we discuss the possible implications of these results to neutrino oscillations.

3.3 Implications to neutrino oscillations

The small $(\mu/e)_{data}/(\mu/e)_{MC}$ ratio suggests two possible oscillation channels, $\nu_\mu \leftrightarrow \nu_e$ and $\nu_\mu \leftrightarrow \nu_\tau$. The constraints on the oscillation parameters are obtained from the sub- and multi-GeV atmospheric neutrino data. For the MC prediction to be compared with the data, we used the fluxes calculated by Honda et al., although no significant difference

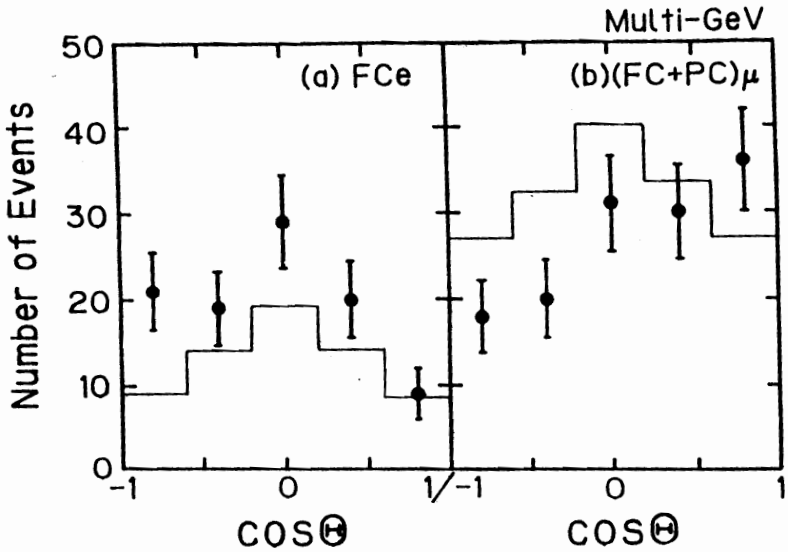

Figure 17:
Zenith-angle distributions for the (a) e-like events and (b) μ-like events (the fully-contained and partially-contained events are combined). The circles with error bars show the data and the histogram the MC (without neutrino oscillations). The downward direction is given by cosΘ =1.

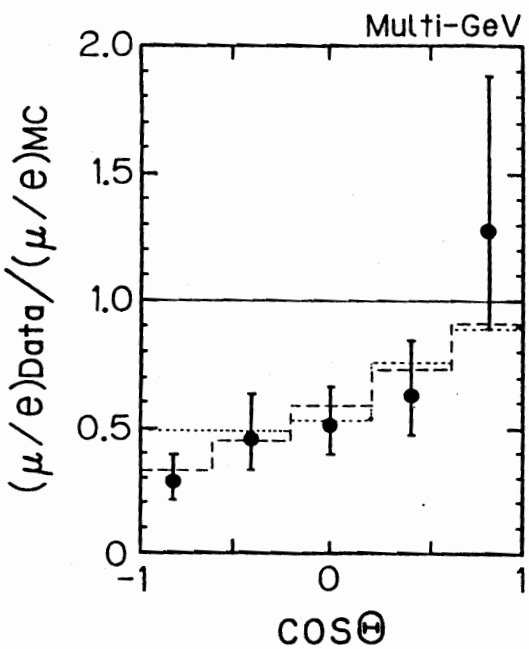

Figure 18:
Zenith-angle distribution of $(\mu/e)_{data}/(\mu/e)_{MC}$, where both the fully-contained and the partially-contained events are included. The circles with error bars show the data. Also shown are the expectations from the MC simulations with neutrino oscillations for parameter sets (Δm^2, $\sin^2 2\theta$) corresponding to the best-fit values to the multi-GeV data for $\nu_\mu \leftrightarrow \nu_e$ ((1.8×10^{-2}eV^2, 1.0), dashes) and $\nu_\mu \leftrightarrow \nu_\tau$ ((1.6×10^{-2}eV^2, 1.0), dots) oscillations.

Table 7:

Sources of systematic error in $(\mu/e)_{data}/(\mu/e)_{MC}$ for the multi-GeV data.

$(\nu_\mu+\overline{\nu}_\mu)/(\nu_e+\overline{\nu}_e)$	<5%	
$\nu/\overline{\nu}$	1%	(*)
$\sigma(CC;\nu_\mu+\overline{\nu}_\mu)/\sigma(CC;\nu_e+\overline{\nu}_e)$	2%	
NC cross section	3%	
Data reduction	3%	(**)
μ/e separation	<4%	(***)
Using multi-ring events	3%	
Vertex position determination	3%	
Absolute energy calibration (inner-counter)	1%	
Absolute energy calibration (anti-counter)	3%	
Non-neutrino background	<1%	
Statistical fluctuation of MC	6%	
Total (added in quadrature)	12%	

(*) 10% error in either the $\nu_e/\overline{\nu}_e$ or $\nu_\mu/\overline{\nu}_\mu$ flux ratio changes the μ/e ratio by 1%.
(**) Uncertainty in the reduction efficiency of partially-contained events.
(***) Error in the μ/e separation affects the numerator and the denominator in μ/e in opposite directions. Thus the systematic error is 2 times <2% misidentification probability.

occurs if the other fluxes are used.

The resultant allowed regions of neutrino-oscillation parameters as obtained from the sub- and multi-GeV data are shown in Fig. 19. From this figure, one may find several important consequences. First, the allowed regions as derived from the sub- and multi-GeV data largely overlap. There is no inconsistency between the sub- and multi-GeV data when interpreting them in terms of neutrino oscillations. Second, the high Δm^2 regions ($\Delta m^2 > 9\times10^{-2} eV^2$ for both the $\nu_\mu \leftrightarrow \nu_e$ and $\nu_\mu \leftrightarrow \nu_\tau$ oscillations) are excluded at 90% C.L. by the present analysis of the multi-GeV data. This is a consequence of the observed zenith-angle dependence.

Since the sub- and multi-GeV data are mutually consistent, allowed regions of neutrino-oscillation parameters are obtained based on all the Kamiokande data. The result is also shown in Fig. 19.

The observed zenith-angle dependence of $(\mu/e)_{data}/(\mu/e)_{MC}$ was shown in Fig. 18. Also shown in the same figure are expectations from the MC simulations for parameter sets (Δm^2, $\sin^2 2\theta$) corresponding to the best fit values for the $\nu_\mu \leftrightarrow \nu_e$ and $\nu_\mu \leftrightarrow \nu_\tau$ oscillations. One sees that the MC predictions which include neutrino oscillations reproduce the data in Fig. 18, and that the observed zenith-angle distribution is consistent with an oscillation interpretation. It should be commented that the agreement between the data and the oscillating MC for the $\nu_\mu \leftrightarrow \nu_e$ channel is slightly better than that for the $\nu_\mu \leftrightarrow \nu_\tau$ channel. This is essentially the result from the $(\mu/e)_{data}/(\mu/e)_{MC}$ ratio smaller than 0.5 in the $\cos\Theta = -1. \sim -0.6$ bin. The question of the possible oscillation channels should be studied in future high-statistics atmospheric-neutrino experiments.

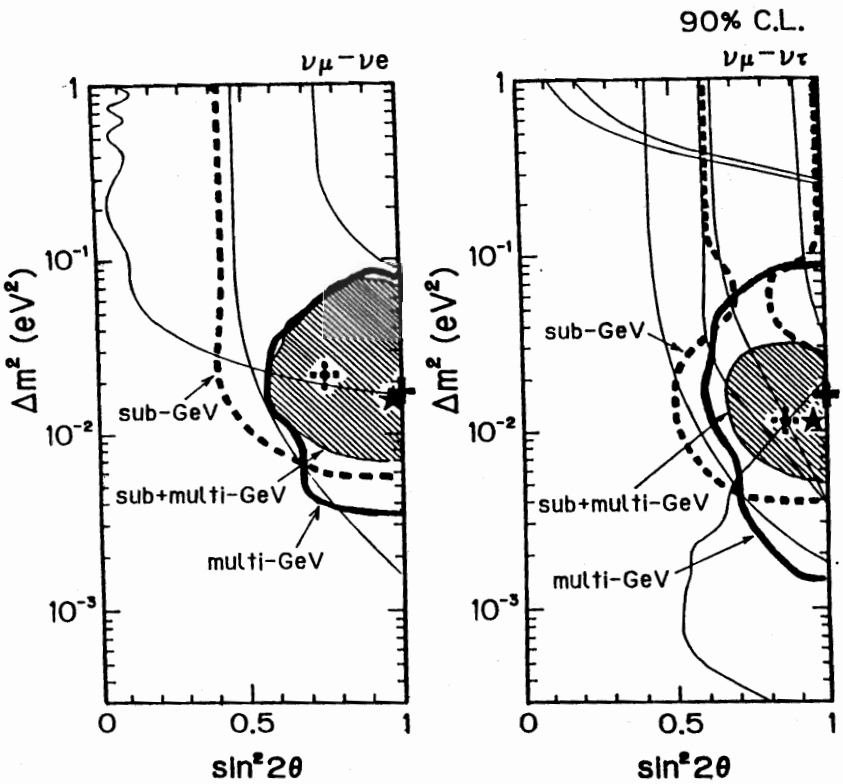

Figure 19:
90% C.L. allowed neutrino-oscillation parameters as obtained from the multi-GeV data (thick curves). 90% C.L. allowed regions as obtained from the sub-GeV data are also shown by thick-dotted curves. The allowed regions as obtained by combining the sub- and multi-GeV data are also shown (shaded region). The best-fit values are also shown by dash-crosses (sub-GeV data), full-crosses (multi-GeV data) and stars (sub- and multi-GeV data combined). The 90% C.L. excluded regions from the other experiments (Frejus, Gosgen, CDHS, Charm, Kamiokande upward-going muons and IMB upward-going muons) are also shown by thin curves.

Fig. 15(a) shows the zenith-angle dependence of $(\mu/e)_{data}/(\mu/e)_{MC}$ for the sub-GeV data. The expected zenith-angle dependences for two sets of neutrino oscillation parameters are also shown in the same figure. Since the zenith-angle distributions are quite different between the sub- and multi-GeV data, it is natural to question if these two distributions are physically consistent or not. Especially, it might be informative to show the zenith-angle distribution of the $(\mu/e)_{data}/(\mu/e)_{MC}$ with different momentum cuts for the sub-GeV data. Figs. 15(b) and (c) show the zenith-angle distributions of the $(\mu/e)_{data}/(\mu/e)_{MC}$ with such cuts. The expected zenith-angle distributions for oscillation parameters are also shown. From these figures and Fig. 18, we see that the zenith-angle distributions of the multi- and sub-GeV data are mutually consistent when the data are interpreted as due to neutrino oscillations.

Table 8:
Atmospheric neutrino data by various underground experiments[25][26][28][27].

Exp.	Data		νMC$^{(*)}$		$\frac{(\mu/e)_{data}}{(\mu/e)_{MC}}$
	e-like	μ-like	e-like	μ-like	
NUSEX	18	32	20.5	36.8	$0.99^{+0.35}_{-0.25}\pm?$
Frejus	57	108	70.6	125.8	$1.06^{+0.19}_{-0.16}\pm 0.15$
Soudan-2	35.3	33.5	28.7	42.1	$0.64\pm0.17\pm0.09$
IMB-3	325	182	257.3	268.0	$0.54\pm0.05\pm 0.12$
Kamiokande (sub-GeV)	248	234	227.6	356.8	$0.60^{+0.06}_{-0.05}\pm0.05$
Kamiokande (multi-GeV)	98	135	66.5	162.2	$0.57^{+0.08}_{-0.07}\pm0.07$

(*) In estimating the event rate, NUSEX, Frejus and Soudan-2 used the flux calculation of Barr et al.[20], while IMB-3 used that of Lee et al.[22], and Kamiokande used that of Honda et al.[21]. The $(\mu/e)_{data}/(\mu/e)_{MC}$ ratio, however, does not depend strongly on the calculation (less than a few % difference).

3.4 Comparison with other experiments and comments on upward-going muon data

Analyses similar to that described above were made by the other underground experiments. Table 8 summarizes the number of observed events for each experiments. Fig. 20 summarizes the observed $(\mu/e)_{data}/(\mu/e)_{MC}$ for each experiment.

The first three experiments, (NUSEX[28], Frejus[26] and Soudan-2[27]), listed in Table 8 and Fig. 20 are tracking calorimeters, and the last two, (IMB-3[25] and Kamiokande), are water Cerenkov detectors. The higher statistics data from the two water Cerenkov detectors agree well for the $(\mu/e)_{data}/(\mu/e)_{MC}$ ratio. The data from NUSEX and Frejus have values closer to unity. However the error bars are large and these data may not repudiate conclusively the results from Kamiokande and IMB-3. The preliminary data from the Soudan-2 experiment are in agreement with the data from the water Cerenkov detectors, although $(\mu/e)_{data}/(\mu/e)_{MC}$ =1 is still allowed at the 2σ level. In several years, the Soudan-2 experiment will accumulate significant number of atmospheric neutrino events, and it will allow an independent check of the small $(\mu/e)_{data}/(\mu/e)_{MC}$ ratio with a different detector technology and systematics.

The multi-GeV data are important for the check of the sub-GeV $(\mu/e)_{data}/(\mu/e)_{MC}$ ratio, and especially for the zenith-angle distribution. At present, multi-GeV data are available only from Kamiokande and Frejus. During 1.56 kton·yr of the exposure, Frejus found for a data sample with visible-energy greater than 1 GeV, $(\mu/e)_{data}/(\mu/e)_{MC}(>1\text{GeV})_{\text{Frejus}} = 1.13^{+0.32}_{-0.25}(\text{stat})$, different from the result obtained by Kamiokande at the 2σ level.

The upward-going muons are produced by CC ν_μ interactions in the rock underneath the detector. If ν_μ oscillate to ν_e or ν_τ, the rate of upward-going muons would be suppressed compared with the case of no oscillations. In the actual experiments, the observed number of events and the zenith-angle distribution are compared with the estimate based

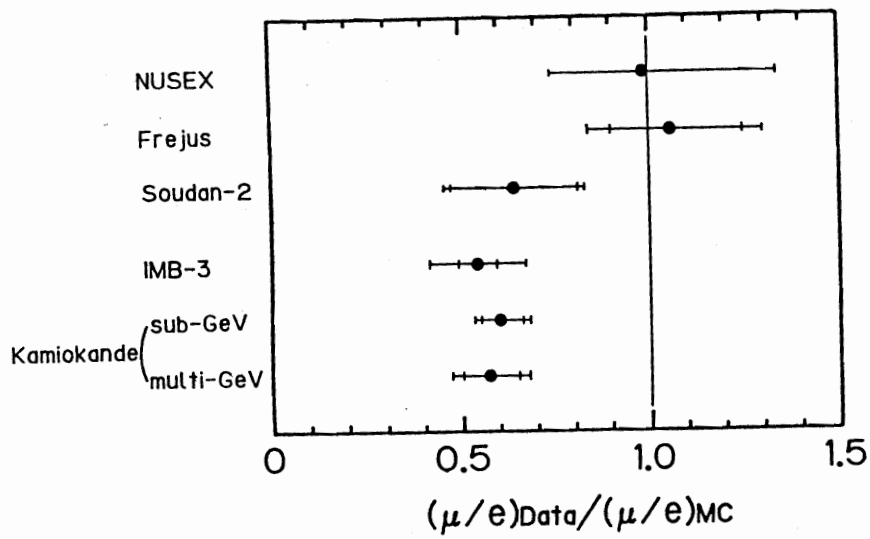

Figure 20:
Measured $(\mu/e)_{data}/(\mu/e)_{MC}$ ratio by various underground experiments[25][26][28][27]. Black circles show the central value, shorter error bars the statistical errors, and longer error bars the total error where statistical and systematic errors are added in quadrature. The systematic error for the NUSEX data is unknown. The data from Soudan-2 are preliminary.

on the Monte Carlo simulation. In order to estimate the flux of upward-going muons, it is necessary to precisely know the flux of atmospheric neutrinos, the neutrino nucleon cross-sections and the dE/dx of muons, all in the range of 1 to 10^5 GeV. Data on upward-going muons and neutrino oscillation parameters obtained from them were published in [29] and [30]. They are carefully discussed in Ref. [31] (see also [29]), which suggests that the excluded parameter regions from upward-going muon data may be changed substantially by future improvements in the very high energy neutrino flux and cross section calculations.

The suggested Δm^2 and $\sin^2 2\theta$ by the present Kamiokande data are $\sim 10^{-2}$eV^2 and ~ 1, respectively. It might be possible to test the neutrino oscillation hypothesis of the atmospheric neutrino data by employing long-baseline accelerator experiments. There should be several combinations of the accelerator and the detector. (For a short summary of this field, see for example Ref. [32].) One possibility is a combination of KEK-PS($<E_\nu>\sim 2$ GeV) and Super-Kamiokande, which have 250 km of baseline length [33]. By these experiments, the whole regions of the allowed parameter regions could be explored.

4 Present status of Super-Kamiokande

The Super-Kamiokande experiment [16] is a natural extension of the Kamiokande experiment with an upgraded performance and a better sensitivity to various measurements. This project was funded in 1991 and the construction started in 1991 and the detector will be ready for physics experiments in April 1996.

One of the physics goals of Super-Kamiokande is the precise measurement of solar and atmospheric neutrino fluxes. For example, the anticipated event rate for ^{8}B solar

neutrino observation is (20~30)/day above E_e =5 MeV.

Much have already been described on the physics potential of the Super-Kamiokande experiment. Here, instead, I would like to describe the present status of the detector construction and the schedule.

The Super-Kamiokande detector is a 50,000 water Cerenkov detector. The size of the detector is 42 m in height and 39 m in diameter. Fig. 21 shows the Super-Kamiokande detector and the related experimental area. The detector consists of two layer of counter, an inner-counter and an anti-counter. The inner-counter is used for the measurement of various phenomena occurring in the fiducial volume of 22,000m^3. 11×10^3 PMTs with 20-inch diameter are used for the measurement of Cerenkov photons. The anti-counter is also a water Cerenkov detector, viewed by 1800 PMTs of 8-inch diameter. The anti-counter is useful for an identification of entering tracks or of the energy leakage from the inner-counter to the anti-counter. The charge and timing information from each PMT are recorded for the physics analysis.

The cavity for the Super-Kamiokande detector was excavated completely in the summer of 1994 at a site 200 m away from the Kamiokande detector. Fig. 22 shows a picture of the Super-Kamiokande cavity taken in August 1994. The on-site construction of the 50,000 m^3 stainless steel tank started in September 1994, and will last until the end of 1995. About 2/3 of the photomultiplier tubes [34] have already been delivered in the Kamioka mine. Dedicated electronics modules which are designed to record charge and timing of any successive events have been developed [35]. Half of the electronics and all of the on-line computers have already been delivered to Kamioka, and they are under testing. A computer facility for the analysis of the Super-Kamiokande data was constructed and started its operation from the beginning of 1994. At present, it is used for the Monte Carlo study of the performance of the Super-Kamiokande detector. The on-site construction of the water purification system will start from Jan. 1995 and will finish March 1995.

The most time- and manpower-consuming part of the detector construction is the installation of PMTs. The installation work will start in the spring of 1995 and will continue until the end of 1995. Then the detector will be filled with pure water. It will take two months to fill the detector with pure water. The experiment will start in April 1996.

5 Summary

Kamiokande has been taking data on solar neutrinos since 1987. The observed flux relative to the SSM prediction of Bahcall and Pinsonneault is 0.48±0.03±0.06. The solar neutrino problem (i.e., the deficit of solar neutrinos) is established by the measurements of the Homestake, Kamiokande, SAGE and Gallex experiments. Data from these experiments also suggest that the flux of ^{7}Be solar ν_e should be much lower than that predicted by the SSM. These data might be explained by the MSW mechanism. Either the non-adiabatic or the large-mixing solution of the MSW mechanism could explain the data. The MSW solutions have three important predictions for future solar neutrino experiments. They are a very low ^{7}Be solar ν_e flux, a distortion of the ^{8}B solar ν_e spectrum or a detectable day-night effect. These predictions should be studied by future solar neutrino experiments

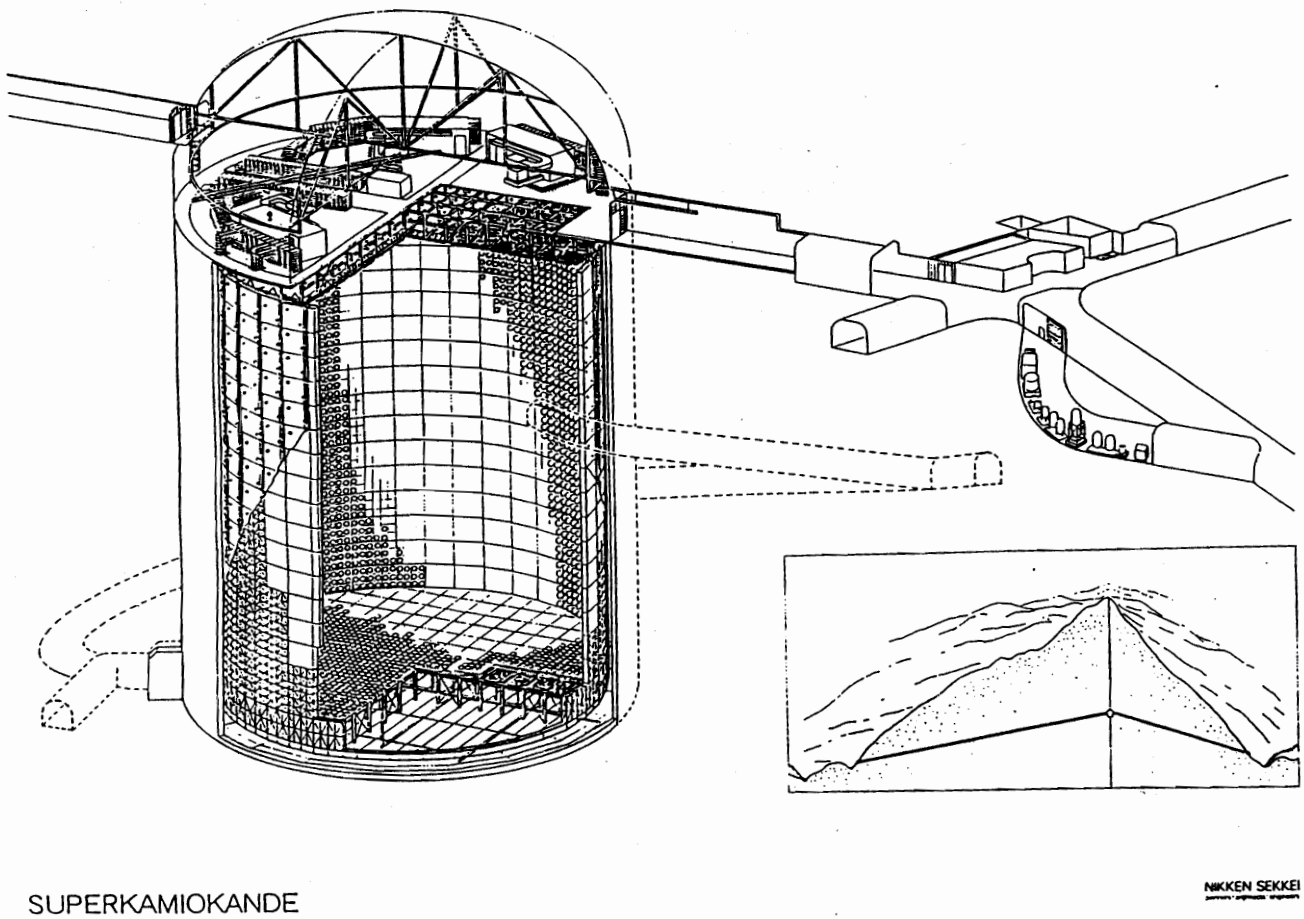

Figure 21:

The Super-Kamiokande detector. The electronics huts and cable trays are sitting on top of the water tank. The water purification system is located at the right in this picture. The access tunnels are also shown. The right-bottom shows the location of the Super-Kamiokande detector in the Ikenoyama-mountain.

such as SNO, Super-Kamiokande and BOREXINO.

Atmospheric neutrinos are measured in Kamiokande. The observed (μ/e) ratio, which is closely related to the atmospheric (ν_μ/ν_e) flux ratio, is $0.60^{+0.06}_{-0.05}\pm0.05$ of the Monte Carlo calculation in the sub-GeV energy range. The IMB-3 and Soudan-2(preliminary) experiments have measured similar (μ/e) values. The energy range of the data from these experiments is mostly in the sub-GeV range. The data in this energy range do not show any significant momentum and zenith angle dependences of the $(\mu/e)_{data}/(\mu/e)_{MC}$ ratio. Recently, Kamiokande published data in the multi-GeV energy range. The observed (μ/e) ratio is $0.57^{+0.08}_{-0.07}\pm0.07$ of the Monte Carlo prediction, in agreement with the sub-GeV data. The zenith angle distribution of the $(\mu/e)_{data}/(\mu/e)_{MC}$ ratio in this energy range shows non-uniform zenith angle dependence, different from the sub-GeV data. The data might be explained by neutrino oscillations. Either $\nu_\mu \rightarrow \nu_e$ or $\nu_\mu \rightarrow \nu_\tau$ oscillation might explain the data. The most likely oscillation parameters are $\Delta m^2 \sim 10^{-2}eV^2$ and

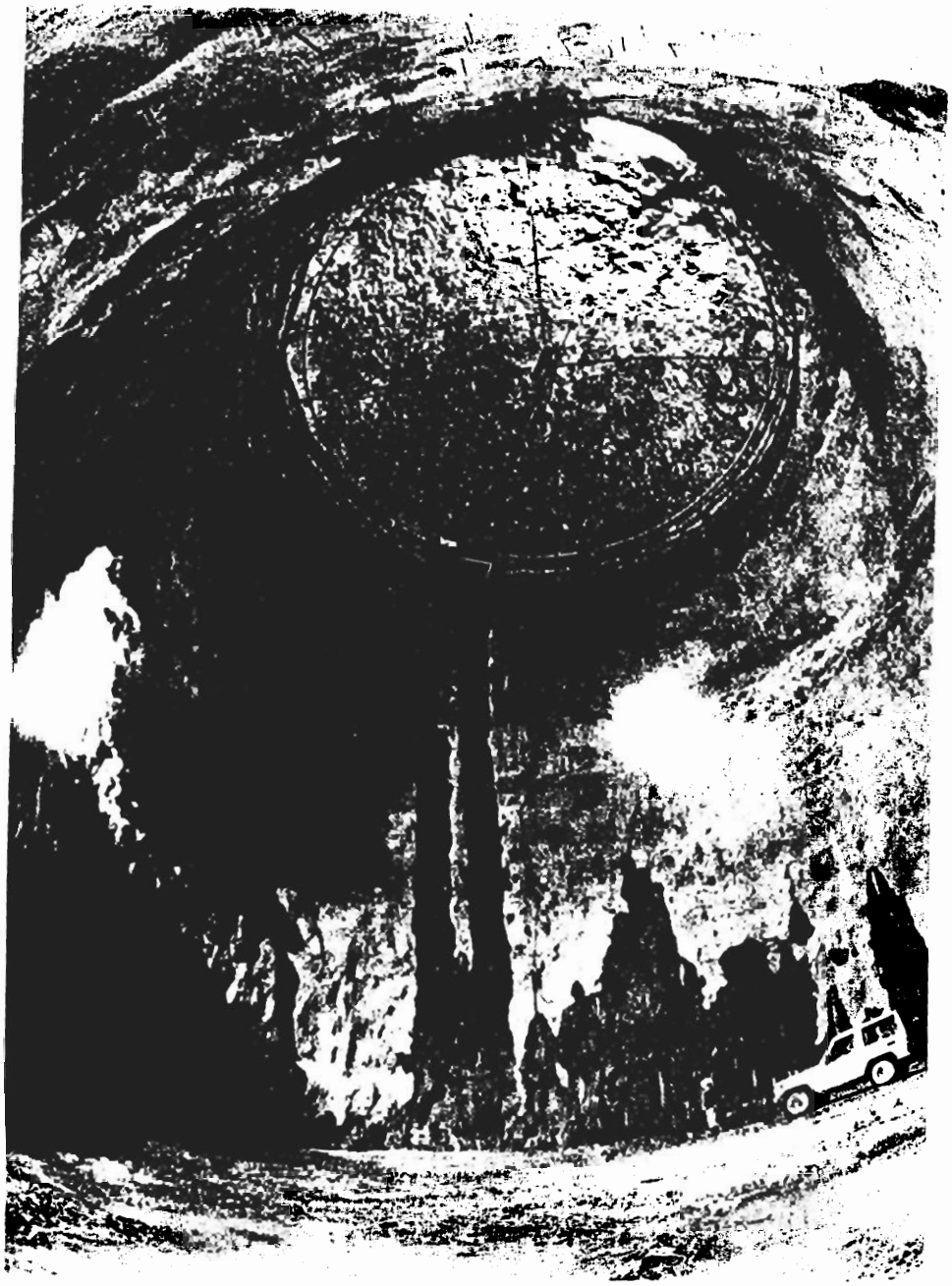

Figure 22:
A picture of the cavity for Super-Kamiokande (August 1994). It has the height of 58 m and diameter of 40 m. A circular crane can be seen at the top (47 m above ground). This crane will be used for the construction of the detector.

$\sin^2 2\theta$ =large. Especially the observed zenith-angle dependence of the $(\mu/e)_{data}/(\mu/e)_{MC}$ ratio in the multi-GeV energy range constrain the allowed Δm^2. Future atmospheric-neutrino experiments or long-baseline neutrino-oscillation experiments should test this important implications on neutrino oscillations. Especially, the future experiments should clarify which of the two possible oscillation channels are the solutions to the atmospheric neutrino problem.

Super-Kamiokande is under construction. It will start experiment in the spring of 1996. We hope Super-Kamiokande will provide useful, new information on the solar and atmospheric neutrino problems.

6 Acknowledgment

I would like to express my deep gratitude to the organizers of this wonderful summer school, in particular, Drs. J.C.Pati and Q.Shafi for their warm hospitality. I am also grateful to many young students of this school who made the school and the stay in Kathmandu very comfortable. Finally, I would like to thank my colleagues in Kamiokande, especially Y.Fukuda, K.Inoue, and Y.Takeuchi, for many useful comments and suggestions.

This work was supported in part by the Japanese Ministry of Education, Science and Culture.

References

[1] A.Suzuki, in "Physics and Astrophysics of Neutrinos", Eds. M.Fukugita and A.Suzuki, Springer-Verlag, Tokyo, 1994, p388.

[2] K.S.Hirata et al., Phys. Rev. Lett. 63 (1989) 16.

[3] K.S.Hirata et al., Phys. Lett. B 220 (1989) 308.

[4] K.S.Hirata et al., Phys. Lett. B 205 (1988) 416.

[5] J.N.Bahcall and R.K.Ulrich, Rev. Mod. Phys. 60 (1988) 297; J.N.Bahcall and M.H.Pinsonneault, Rev. Mod. Phys. 64 (1992) 885.

[6] S.Turck-Chieze et al, Astrophys. J. 335 (1988) 415; S.Turck-Chieze and I.Lopes, Astrophys. J. 408 (1993) 347.

[7] K.S.Hirata et al., Phys. Rev. D 44 (1991) 2241: Y.Suzuki (for the Kamiokande collaboration), talk presented at Neutrino '94, the XVI International Conference on Neutrino Physics and Astrophysics, Eilat, Israel, May–June 1994.

[8] R.Davis Jr., in Proc. of the International Symposium on Neutrino Astrophysics, Takayama/Kamioka, Japan, 1992, p47.

[9] J.N.Abdurashitov et al., Phys. Lett. B 328 (1994) 234.

[10] P.Anselmann et al., Phys. Lett. B 327 (1994) 377.

[11] See for example, John N. Bahcall and H. A. Bethe, Phys. Rev. Lett. 65 (1990) 2233.

[12] S.P.Mikheyev and A.Yu.Smirnov, Sov. J. Nucl. Phys. 42 (1985) 913; L.Wolfenstein, Phys. Rev. D 17 (1978) 2369; ibid. 20 (1979) 2634.

[13] N.Hata and P.Langacker, Phys. Rev. D 50 (1994) 632.

[14] K.S.Hirata et al., Phys. Rev. Lett. 66 (1991) 9.

[15] G.T.Ewan et al., "Sudbury Neutrino Observatory Proposal", SNO-87-12, 1987; "Scientific and Technical Description of the Mark II SNO Detector", edited by E.W.Beier and D.Sinclair, SNO-89-15, 1989.

[16] M.Koshiba and Y.Totsuka, Proc. of Workshop: Toward Unification and its Verification, KEK Report (1984): Y.Totsuka, Proc. of 7th Workshop on Grand Unification/ICOBAN '86, Toyama (1986).

[17] "BOREXINO at Gran Sasso — proposal for a real time detector for low energy solar neutrinos", edited by G.Bellini, M.Campanella, D.Giugni, and R.Raghavan (1991).

[18] K.Nishikawa (for the Kamiokande collaboration), talk presented at Neutrino '94, the XVI International Conference on Neutrino Physics and Astrophysics, Eilat, Israel, May–June 1994.

[19] M.Nakahata et al., J. Phys. Soc. Jpn. 55 (1986) 3786.

[20] G.Barr, T.K.Gaisser and T.Stanev, Phys. Rev. D 39 (1989) 3532.

[21] M.Honda, K.Kasahara, K.Hidaka and S.Midorikawa, Phys. Lett. B 248 (1990) 193.

[22] H.Lee and Y.S.Koh, Nuovo Cimento 105B (1990) 883.

[23] E.V.Bugaev and V.A.Naumov, Phys. Lett. B 232 (1989) 391.

[24] L.V.Volkova, Sov. J. Nucl. Phys. 31 (1980) 784.

[25] D.Casper et al., Phys. Rev. Lett. 66 (1991) 2561; R. Becker-Szendy et al., Phys. Rev. D. 46 (1992) 3720.

[26] Ch. Berger et al., Phys. Lett. B 227 (1989) 489; 245 (1990) 305.

[27] P.Litchfield, for the Soudan 2 Collaboration, Proc. of the International Workshop on ν_μ/ν_e Problem in Atmospheric Neutrinos, Laboratori Nazionali del Gran Sasso, Italy, March 1993, p114: M.C.Goodman, for the Soudan 2 Collaboration, Preprint PDK-600 (1994), to appear in Proceedings of Neutrino '94, International Conference on Neutrino Physics and Astrophysics, Eilat, Israel, May—June 1994.

[28] M.Aglietta et al., Europhys. Lett. 8 (1989) 611.

[29] Y.Oyama et al., Phys. Rev. D 39 (1989) 1481.

[30] R.Becker-Szendy et al., Phys. Rev. Lett. 69 (1992) 1010.

[31] W. Frati, T.K.Gaisser, A.K.Mann and T.Stanev, Phys. Rev. D 48 (1993) 1140.

[32] Jean-Pierre Revol, CERN-PPE/93-84 (1993); Stephen Parke, Fermilab-Conf-93/056-T (1993).

[33] K.Nishikawa, INS-Rep.-924, (1992).

[34] A.Suzuki et al., Nucl. Inst. Meth. in Phys. Res. A329 (1993) 299.

[35] T.Tanimori et al., IEEE Trans. Nucl. Sci. 36 (1989) 497: H.Ikeda et al., Nucl. Inst. Meth. in Phys. Res. A320 (1992) 310.